Available online at www.sciencedirect.com
ScienceDirect
ELSEVIER
Ultramicroscopy 107 (2007) 1186–1193
ultramicroscopy
www.elsevier.com/locate/ultramic

The Peak Pairs algorithm for strain mapping from HRTEM images

Pedro L. Galindo[a,*], Sławomir Kret[b], Ana M. Sanchez[c], Jean-Yves Laval[d], Andrés Yáñez[a], Joaquín Pizarro[a], Elisa Guerrero[a], Teresa Ben[c], Sergio I. Molina[c]

[a]*Departamento de Lenguajes y Sistemas Informáticos, CASEM, Universidad de Cádiz, Pol. Rio San Pedro s/n. 11510, Puerto Real, Cadiz, Spain*
[b]*Institute of Physics, PAS, AL. Lotników 32/46, 02-668 Warszawa, Poland*
[c]*Departamento de Ciencia de los Materiales e Ing. Metalúrgica y Q. Inorgánica, Facultad de Ciencias, Universidad de Cádiz, Pol. Rio San Pedro s/n. 11510, Puerto Real, Cadiz, Spain*
[d]*Laboratoire de Physique du Solide, UPR5 CNRS-ESPCI, Paris, France*

Received 6 July 2006; received in revised form 18 January 2007; accepted 31 January 2007

Abstract

Strain mapping is defined as a numerical image-processing technique that measures the local shifts of image details around a crystal defect with respect to the ideal, defect-free, positions in the bulk. Algorithms to map elastic strains from high-resolution transmission electron microscopy (HRTEM) images may be classified into two categories: those based on the detection of peaks of intensity in real space and the Geometric Phase approach, calculated in Fourier space. In this paper, we discuss both categories and propose an alternative real space algorithm (*Peak Pairs*) based on the detection of pairs of intensity maxima in an affine transformed space dependent on the reference area. In spite of the fact that it is a real space approach, the *Peak Pairs* algorithm exhibits good behaviour at heavily distorted defect cores, e.g. interfaces and dislocations. Quantitative results are reported from experiments to determine local strain in different types of semiconductor heterostructures.
© 2007 Elsevier B.V. All rights reserved.

PACS: 68.37.−d; 68.55.−a

Keywords: Strain mapping; High-resolution transmission electron microscopy (HRTEM); Data processing/image processing

1. Introduction

Due to the increasing importance of the quantitative stress and strain measurements at atomic scale, a large amount of research has been carried out to speed up techniques over the last decade. The development of nanotechnology has been stimulated by the microelectronics industry, which has pursued the optimisation and miniaturisation of devices. Since the device properties depend on composition control in three dimensions, the structural characterisation by high-resolution transmission electron microscopy (HRTEM) constitutes a potential breakthrough to optimise heteroepitaxial systems, allowing quantitative measurements at subnanometric level.

Recent advances in digital imaging and image-processing techniques, together with improved point-to-point resolution of microscopes have offered the possibility of locally determining the elastic strain of materials at subnanometric scale using HRTEM images. However, the reliability of strain mapping determination relies on the assumption of a constant spatial relationship between the intensity maxima in the HRTEM micrograph and the relative positions of the atomic columns in the specimen. Due to some known effects, such as thin foil relaxation, local crystal tilts and thickness and/or composition variation across the material, the reliability of these strain measurements is somewhat problematical [1,2].

A detailed analysis of the impact of such effects on the accuracy of lattice-distortion analysis in the case of the

*Corresponding author. Tel.: +34 956 016434; fax: +34 956 016437.
E-mail address: pedro.galindo@uca.es (P.L. Galindo).

0304-3991/$ - see front matter © 2007 Elsevier B.V. All rights reserved.
doi:10.1016/j.ultramic.2007.01.019

InP/GaInP QDs is given in Ref. [3]. Additionally, the microscope transfer function affects the phases of the diffracted beams differently depending on their position in Fourier space which can give rise to strain artefacts [4]. In the case of strained heterostructures, the effect of column bending needs to be carefully considered. As can be shown by simulations, which take into account most of these effects, the average strain of thicker layers can be determined with sufficient accuracy [5]. In order to determine strain field mapping, several methodologies have been described in the literature, which are based mainly on two different approaches, *Peak Finding* and *Geometric Phase Analysis*.

Peak-finding (PF) methods [6–13] work in real space, superimposing a two-dimensional reference lattice extrapolated from a non-distorted region of the material to the experimental one, built up from the set of intensity maxima in the HRTEM image, and calculating the local discrete displacement field at each node. Subsequently, by derivating the calculated displacement field, the strain field is obtained.

On the other hand, Geometric Phase (GP) methodology [14] works in Fourier space, and consists of filtering the image with an asymmetric filter centred on a Bragg spot in the Fourier transform of an HRTEM lattice image and performing an inverse Fourier transform. The phase component of the resulting complex image gives information about local displacements in a direction corresponding to the normal to lattice fringes corresponding to position of the Bragg spot. Local strain field components are calculated by derivation of the displacement obtained from two non-collinear Fourier components. As well symmetric and rotation components of distortion can be simply calculated from these derivates.

Peak-finding approaches have some advantages, such as less demanding memory and CPU requirements, given that bidimensional complex Fourier transforms are not needed at all. This is not true in the case when noise reduction is made in Fourier space. On the other hand, *Geometric Phase* has shown to be very useful when determining strain mapping in areas containing defects, such as dislocations [4,14].

Since both methods are noise sensitive, noise reduction usually improves the accuracy in subsequent strain determination. Low signal-to-noise ratios may produce undesired effects in any case. Peak-finding methods might have problems because noise may even prevent the lattice from being built, while the Geometric Phase method cannot stand over-sampling, which results in Bragg spots being too close to the zero frequency for adequate filtering.

Even when the intensity maxima can be easily detected in the case of highly deformed areas, local amorphisation or local contrast problems (for example due to local thickens variation) in *Peak Pairs* (PP) algorithm the automatic image girding usually fail and need human intervention to construct correctly continuous lattice.

In this paper, we introduce a real space approach, PP, which is based on the detection of pairs of intensity maxima in the affine transformed space dependant on the reference area. Despite it is a real space approach, the PP algorithm has been successfully applied to areas containing defects, and therefore, it is an appropriate approach in the real space to obtain strain field mapping not only in pseudomorphical heterostructures but also at interfaces in plastically relaxed systems and defective regions, such as dislocated areas and areas with inverse contrasts that occur usually in experimental images due to local foil thickness changes or narrow chemical gradients. In this paper, we will only discuss performance of PP image-processing algorithms in relation to the GP method on arduous images and not absolute distortion field present in the sample which needs additional modelling steps.

2. PP approach

As a preliminary step, the reduction of noise is a very important issue, allowing us to improve the resolution limit by a factor of 2–4 [8], and Wiener filtering [15] can be a good approach. The Wiener filter is a type of linear filter that is applied to an image adaptively, tailoring itself to the local image variance, and preserving edges and other high-frequency parts of the image, assuming Gaussian white additive noise. It applies a low-pass filter to the image using neighbourhoods of size m-by-n to estimate the local image mean and standard deviation, creating a pixel-wise Wiener filter with these estimates. Excellent results are obtained by fairly rough estimates of the filter, because the optimal filter results from a minimisation method, and therefore, the quality of the results differs only from the true optimum by an amount that is second order, with the precision to which the filter is determined [16].

In order to obtain a fringe image instead of the dot pattern, a Bragg filter is applied to the Fourier-transformed image. Bragg filtering consists of placing a mask around one or more Bragg peaks in the Fourier transform of the image and then apply an inverse Fourier transform. The size of the kernel mask determines the range of frequencies that are removed by the filter. Although Bragg filtering is easy to carry out, it may, in the case of low signal-to-noise images, induce artefacts which mostly depend on the diameter of the filtering mask that is applied. If the mask used for the filtering is too small, relevant information such as local non-periodic details may be lost. In particular, the information from the strongly deformed but small areas can be cut off by filtering because signal is weak in the Fourier space from such zones blurred in the noise coming from the whole image. On the other hand, larger masks produce noisy images.

The first stage in the procedure consists of the detection of local intensity maxima in the filtered image. Local maxima are defined as the pixels of a given intensity (I_0) whose external boundary pixels all have a value lower than I_0, i.e. using an 8-connected neighbourhood. Local maxima are identified on a pixel basis on the Bragg-filtered image,

so its maximum resolution is 1×1 pixel. In order to obtain subpixel resolution, we consider initially two approaches: 2D interpolation (linear, spline, polynomial) and function maximisation. 2D interpolation requires a sampling of the image at fractional locations, generating matrices of values at subpixel resolution, at which to interpolate the data. The higher the required precision, the higher the dimension of the matrices will be, thus increasing the computational requirements to process a given image. Once the image has been interpolated, it is easy to determine the coordinates of the maximum intensity at subpixel resolution. The second approach requires less computational effort, but it assumes that the local shape of grey values around a peak follows a 2D parametric function. We propose to fit a 2D quadratic function using an 8-connected neighbourhood of two pixels around each local maximum: $z(x,y) = ax^2 + by^2 + cxy + dx + ey + f$. Once the quadratic function has been fitted to the neighbourhood of a peak, the maximum of this function is easily determined by setting derivatives to 0 as follows:

$$\frac{\partial z}{\partial x} = 0, \qquad \frac{\partial z}{\partial y} = 0 \quad \Rightarrow \quad \begin{vmatrix} 2a & c \\ c & -2b \end{vmatrix} \begin{vmatrix} x_{\max} \\ y_{\max} \end{vmatrix} = \begin{vmatrix} -d \\ -e \end{vmatrix}.$$

This allows us to determine precisely the peak ($x_{\max}$, $y_{\max}$) at subpixel resolution. This approach is more sensitive to noise, but it has shown to be much faster than interpolation, achieving enough precision in the experiments. If a higher precision is desired at the cost of increasing the time taken for calculations, bicubic interpolation [16] may be a good approach.

The second step is to determine two non-collinear basis vectors that will define the position of the peaks of maximum intensity in the reference area, by selecting three points, A, B and C, that will define vectors $\vec{a} = \overline{\mathrm{AB}} = (a_x, a_y)$ and $\vec{b} = \overline{\mathrm{AC}} = (b_x, b_y)$, as shown in Fig. 1. Therefore, in the reference area, intensity maxima are supposed to be located at positions $\mathrm{A} + m \cdot \vec{a} + n \cdot \vec{b}$, with m and n denoting integers. These vectors will be used as the reference at which the strains of the specimen are determined. The reference area should be taken on the same image, but far away from deformed regions.

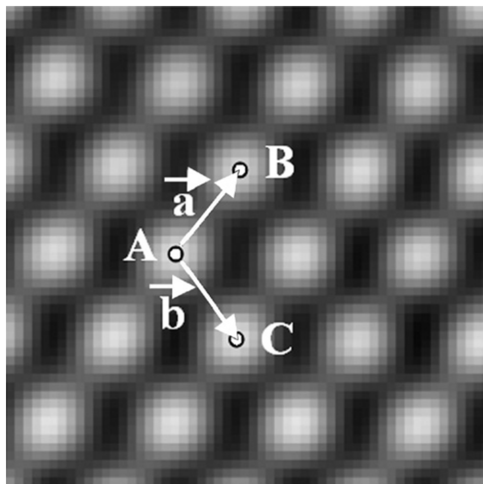

Fig. 1. Basis vectors $\vec{a} = (a_x, a_y)$ and $\vec{b} = (b_x, b_y)$ defined in the reference area by points A, B and C. (a) [1 1 0] HRTEM image of CdTe, showing the chosen pair of basis vectors (magnitude = $5x$). (b) Affine transformed intensity maxima, showing transformed basis vectors and a dislocation in the x direction.

An *affine transformation* maps variables (e.g. pixel intensity values located at position (x, y) in an input image) into new variables (x', y'). The main advantage of affine transformations is that lines and parallelism are preserved, and therefore are well suited to the transformation of crystalline images. An affine transformation is defined as a linear combination of four primitives: translation, rotation, scaling and reflection, and may be described mathematically as

$$\begin{bmatrix} x' \\ y' \end{bmatrix} = \begin{bmatrix} a & b & c \\ d & e & f \end{bmatrix} \begin{bmatrix} 1 \\ x \\ y \end{bmatrix}.$$

In order to determine precisely the transformation matrix, we must have at least three non-collinear control points, because three points provide six values, which can be used to solve the six unknowns (i.e. a, b, c, d, e and f). We define the following control points: coordinates of point A should be transformed into (0, 0), vector (a_x, a_y) into (1, 0) and vector (b_x, b_y) into (0, 1). The solution of the resulting linear system is the desired solution, calculated as follows:

$$\begin{bmatrix} 0 & 1 & 0 \\ 0 & 0 & 1 \end{bmatrix} = \begin{bmatrix} a & b & c \\ d & e & f \end{bmatrix} \begin{bmatrix} 1 & 1 & 1 \\ A_x & a_x & b_x \\ A_y & a_y & b_y \end{bmatrix},$$

and therefore, the transformation matrix is easily obtained:

$$\begin{bmatrix} a & b & c \\ d & e & f \end{bmatrix} = \begin{bmatrix} 0 & 1 & 0 \\ 0 & 0 & 1 \end{bmatrix} \begin{bmatrix} 1 & 1 & 1 \\ A_x & a_x & b_x \\ A_y & a_y & b_y \end{bmatrix}^{-1}.$$

In the case of a non-distorted material, this transformation would generate a perfectly square grid, where the maxima of the reference area will be located at integer coordinate values in the affine transformed space. In an experimental image, we obtain a near-square grid where it is easy to identify deviations with respect to the grid defined by the basis vectors, being therefore very easy to identify defects in the material. Fig. 2a shows a Bragg-filtered HRTEM image of a dislocation in CdTe, as well as the chosen basis vectors (magnitudes have been multiplied by 5) that define the affine transformation to be applied. Once the intensity maxima in the Bragg-filtered HRTEM image are identified, their corresponding coordinates are affine transformed. Fig. 2b shows the peaks' positions in the transformed space, clearly revealing the presence of a dislocation in the material (i.e. extra-plane of maxima can be easily observed in the figure, indicating the position of the dislocation in the material).

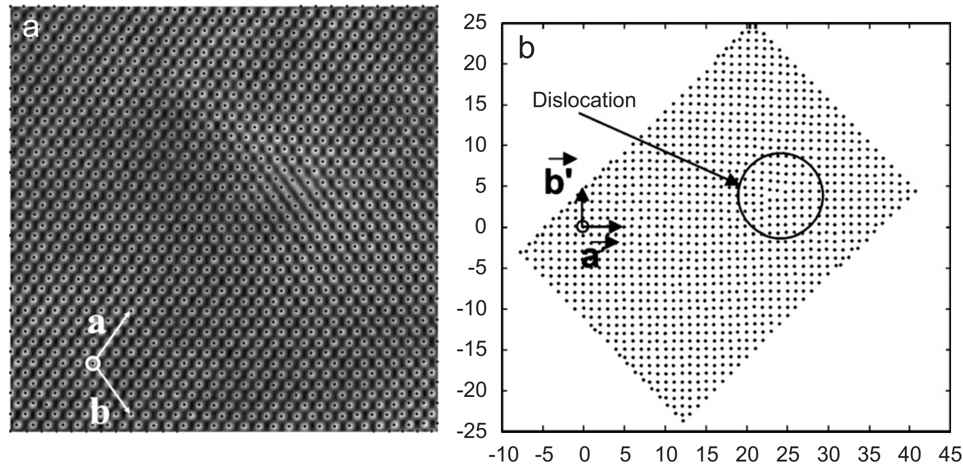

Fig. 2. (a) HRTEM image of a dislocation inside the CdTe material (b) Affine transformation defined by reference vectors $\vec{a}$ (a_x, a_y) and $\vec{b}$ (b_x, b_y).

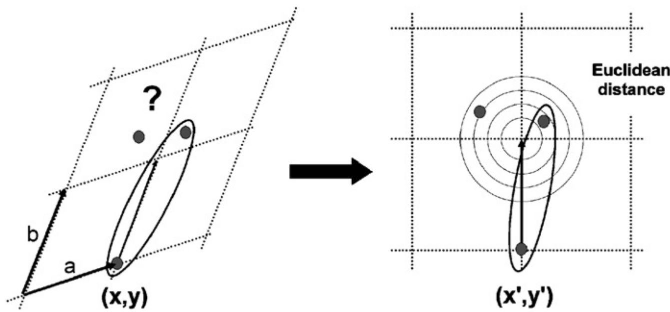

Fig. 3. Affine transformation defined by reference vectors $\vec{a}$ (a_x, a_y) and $\vec{b}$ (b_x, b_y). This transformation allows the use of Euclidean distance when searching the optimal "partner" of a given peak.

The next step in the procedure is the identification of Pairs of Peaks using the chosen basis vectors and the intensity maxima set in the image. For each intensity maximum (x, y), we look for its associated peaks in the direction of the basis vectors ($\vec{a}$ and $\vec{b}$) and at a distance of $|\vec{a}|$ and $|\vec{b}|$, respectively. In the transformed space, this corresponds to locating the nearest peaks to $(x'+1, y')$, $(x'-1, y')$, $(x', y'-1)$, $(x', y'+1)$, and considering them as neighbours of (x', y'), given that transformed reference vectors correspond to orthogonal unit vectors, as shown in Fig. 3.

The intensity maxima coordinates in the transformed space allow us to use the Euclidean distance in order to determine the *most probable* "partner" of a given maximum of intensity in the peak pair's identification stage, assuming Gaussian probability distributions centred at the peaks and considering equal covariance matrices.

By connecting pairs of neighbours by single lines, different types of dislocations have been detected both along the CdTe/GaAs interface (Figs. 4b-1 and b-2) and inside the CdTe material (Fig. 4b-3).

The identification of pairs of peaks along two non-collinear directions enables us to determine precisely the strain field. Let us consider a pair of neighbours in the direction of vector $\vec{a}$, formed by peaks $\text{Peak}_0 = (x_0, y_0)$ and $\text{Peak}_1 = (x_1, y_1)$. From these vectors, it is easy to calculate

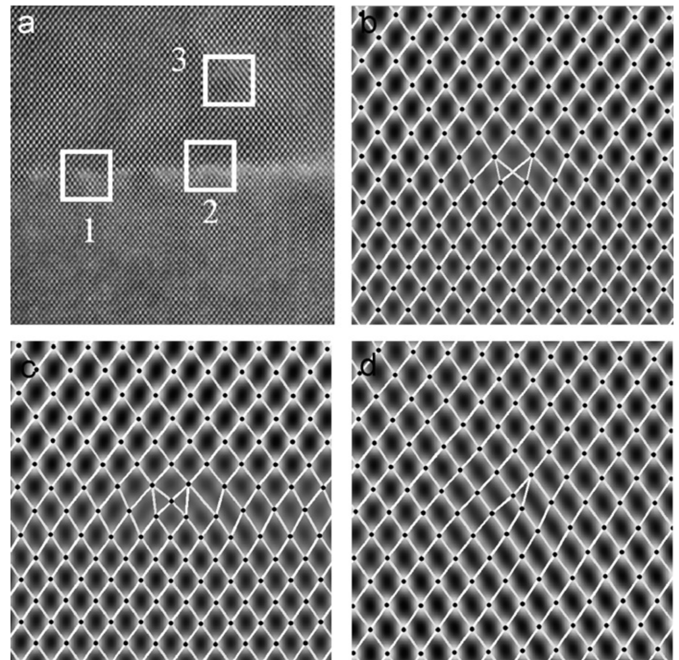

Fig. 4. (a) HRTEM image of a CdTe/GaAs interface (see Fig. 5) showing three different areas of interest containing different types of dislocations. (b) Pair identification using PP around different dislocations: two along the interface (1 and 2) and another one inside the CdTe material (3).

displacements in the material, using $u_x = x_1 - x_0 - a_x$ and $u_y = y_1 - y_0 - a_y$. The same calculations apply to the calculation of v_x and v_y, but considering the second basis vector ($\vec{b}$). A diagram showing these relationships is shown in Fig. 5.

The strain field components can be calculated by solving the following set of linear equations:

$$\left.\begin{aligned} u_x &= a_x e_{xx} + a_y e_{xy} \\ u_y &= a_y e_{yy} + a_x e_{yx} \\ v_x &= b_x e_{xx} + b_y e_{xy} \\ v_y &= b_y e_{yy} + b_x e_{yx} \end{aligned}\right\} \qquad \begin{bmatrix} e_{yx} \\ e_{yy} \end{bmatrix} = \begin{bmatrix} a_x & a_y \\ b_x & b_y \end{bmatrix}^{-1} \begin{bmatrix} u_y \\ v_y \end{bmatrix}, \quad \begin{bmatrix} e_{xx} \\ e_{xy} \end{bmatrix} = \begin{bmatrix} a_x & a_y \\ b_x & b_y \end{bmatrix}^{-1} \begin{bmatrix} u_x \\ v_x \end{bmatrix},$$

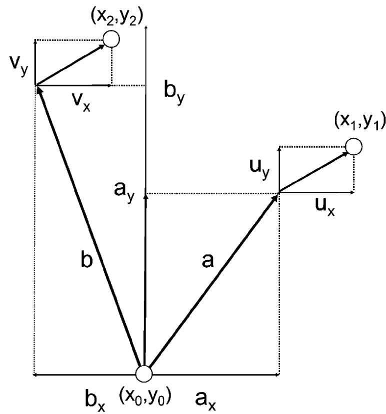

Fig. 5. Diagram of the calculation of distortions $u = (u_x, u_y)$ and $v = (v_x, v_y)$ from two non-collinear pairs.

where (u_x, u_y) and (v_x, v_y) are the coordinates of the displacement with respect to reference vector $\vec{a} = (a_x, a_y)$ and $\vec{b} = (b_x, b_y)$, respectively, and e_{xx}, e_{xy}, e_{yy} and e_{yx} are defined as follows:

$$e_{xx} = \frac{\partial u}{\partial x}, \qquad e_{xy} = \frac{\partial u}{\partial y}, \qquad e_{yy} = \frac{\partial v}{\partial y}, \qquad e_{yx} = \frac{\partial v}{\partial x}.$$

Once the lattice strain tensor for each maximum is calculated, the continuous distortion field can be determined at any point using a 2D interpolation process.

The essential difference in the whole procedure with respect to "standard" peak finding is that PP measures strain using pairs of peaks detected in the affine transformed space, instead of fitting a distorted lattice to a set of peaks and compare it with respect to a reference lattice. This different approach has several advantages. First, the errors introduced in fitting a regular lattice to a deformed set of peaks are avoided. This is especially important in the presence of dislocations, where the fit is not easy, and any error may be propagated across the lattice. On the other hand, PP measures local distortions with respect to the reference basis vectors. Any error keeps local, and is not propagated because no lattice is deployed. Second, strain around defects can be determined without user's intervention. The determination of neighbours in the affine transformed space provides a significant reduction of errors in detecting adjacent peaks in the direction of basis vectors in heavily distorted areas.

A technical constraint of the proposed technique is that the strain field can be determined by interpolation exclusively in the convex hull formed by all the peaks detected in the image. Outside this area, usually close to the borders, strain values are not valid.

3. Experimental details

HREM cross-section specimens were prepared from a thick CdTe film grown by molecular beam epitaxy (MBE) on (1 0 0) GaAs 2° misoriented substrate. The high-resolution electron microscopy was performed by using a Philips CM 20 UT microscope operating at 200 kV with a point resolution of 0.19 nm. For HRTEM observation, an aperture of 11 nm^{-1} (including nine beams: 000, 4×111, 2×220, 2×200) was used for image formation. The thickness of the foil for which the images were analysed was uniform and estimated to be below 15 nm. Simulated images of GaAs and CdTe crystals along the [1 1 0] zone axis show that close to Scherzer defocus and for foil thicknesses between 5 and 15 nm the simple contrast condition when the bi-atomic column positions are represented by white or black dots can be easily achieved. In practice, the defocus value was slightly tuned to keep homogeneous contrast (with bright dots on a dark background) for GaAs and CdTe crystal in the whole-observed area.

In order to improve the signal-to-noise ratio, in the 2048×2048 pixels HREM experimental image shown in Fig. 6, a Wiener filter was applied, followed by a Bragg filter designed using a Gaussian-shaped mask kernel (size = 35×35 pixels) centred at $\bar{1}\,\bar{1}\,1$ and $1\,\bar{1}\,1$ "structural reflections".

4. Comparison of PP and GP techniques

In order to test the PP algorithm, HRTEM micrographs corresponding to different nanostructures, both in pseudomorphical growth and containing structural defects, have been analysed. Strain mapping results have been compared with those obtained using GP, as it is the most widely used approach to strain mapping from HRTEM images in the presence of defects. Experimental results for GP have been obtained using GP scripts by Hÿtch [14]. For PP, we have developed a specific software package, called Strain Determination Software. This package works under MATLAB [17], and it is available from our web page [18].

Dislocations have always been an obvious and fruitful field of application for strain mapping. The *PP* procedure was first applied to an HRTEM image of a CdTe/GaAs interface along the [1 1 0] zone axis containing an array of misfit dislocations, shown in Fig. 6. The automatically reconstructed lattice from PP and GP analysis are shown in Fig. 7.

The dislocation on this interface was previously analysed by the dislocation core distribution method derived from GPA in [19]. Although *PP* algorithm works in real space and *GP* in the reciprocal one, both methods provide similar strain maps. A previous real space approach for strain mapping around defects was published by Rosenauer [20], but neighbouring peaks at the interface were not automatically determined. PP procedure is, to our knowledge, the first real space strain mapping algorithm providing comparable results to GP in the presence of defects without the need of user's intervention. Because of space limita-

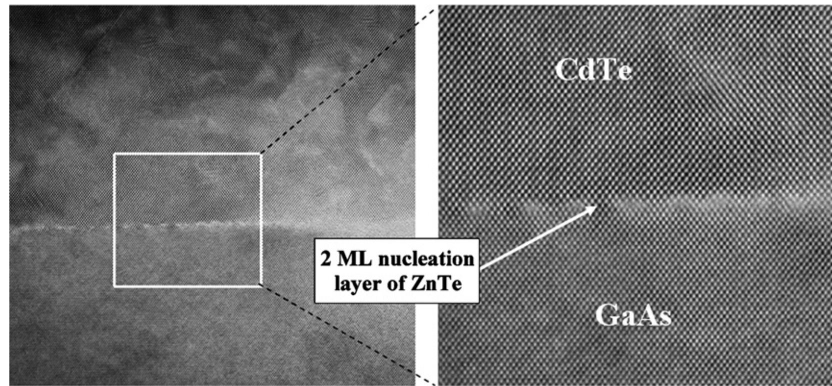

Fig. 6. [1 1 0] HRTEM image of a CdTe/GaAs interface.

Fig. 7. CdTe/GaAs interface strain maps obtained by PP and GP from the HRTEM image in Fig. 5. (a) PP-e_{xx} (b) GP-e_{xx} (c) PP-e_{xy} (d) GP-e_{xy}.

tions, only strain maps e_{xx} and e_{xy} are shown, but those corresponding to e_{yy} and e_{yx}, give equally similar results.

Both, GP and PP strain maps were calculated using the $\bar{1}\,\bar{1}\,1$ and $1\,\bar{1}\,1$ "structural reflections". Let us note that these two reflections are enough to produce a spot pattern in real space. However, in PP we could have used additional reflections, such as $\bar{2}\,0\,0$. This would have produced a similar spot pattern where peak positions better fit the original image. We may even increase the number of reflections considering those with higher spatial frequency, such as $2\,0\,0$ and $0\,2\,2$. This generates a spot pattern with more information as compared to two reflections approach. However, this also produces an increment of noise and these higher frequency periodicities can introduce information which can be more affected by electron optics due to their higher spatial frequencies. Generally it is difficult to choose conditions where many reflections are in the relatively flat region of the Phase Transfer Function and their use it is not recommended. Given that GP only uses two reflections, we have used the same set of reflections in both algorithms (GP and PP) in order to be able to compare their results.

In deformation measurement by image processing the most important factor is the global averaging which depends on the diameter of the mask in GP method and "the force" of the Wiener Filter which depends mainly on the noise estimator. In PF and PP algorithms, the global averaging of deformation is only imposed by Wiener filter because the whole area of Fourier space, where we can expect useful information even far away from Bragg peaks, can be considered in the filtered image. In GP, the size of the mask is limited by the distances between Bragg peaks. Results from Fig. 7 show that the distortion around defect looks similar for both methods.

Without simulation, taking into account "real world" effects, we cannot prove that the shown distributions correspond to real deformations of the crystal for complicated configurations with the presence of Ga, As, Zn, Cd, Te atoms and possible misalignment of the microscope and/or the sample, surface non-homogeneous relaxation, etc., but these aspects are not the object of the current work. The minor differences between results obtained by GP and PP method are attributed to the differences in the spatial frequencies and their information content and the interpolation algorithms used in PP.

5. Discussion

Experimental results allow us to conclude that PP algorithm is an alternative method to GP. Let us note that both algorithms fail in the determination of strain near the borders of the image. In the case of GP, the border effects are due to spectral leakage. On the other hand, PP is based in the determination of strain at a finite set of points, followed by an interpolation process. Therefore, outside the region where peaks lay, strain values are extrapolated and may be inaccurate. However, in experimental images, this problem is negligible, given that areas of interest, such as dislocations, interfaces and so on, might be centred in the middle of the image.

From the analysis when comparing GP and PP, we conclude that:

- Both algorithms give similar results in the proximity of defects. This property is very interesting in the analysis of defective nanostructures.
- PP works in real space. This property leads to some advantages, such as reduced memory and CPU requirements, given that bidimensional complex Fourier transforms are not needed at all. This allows the calculation of strain maps of greater images, that is to say, wider areas and/or higher resolution. Noise reduction will usually be in this case the most demanding procedure of the whole strain mapping process.
- PP allows us to use more than two beams in order to determine the strain. However, we should be careful, because as the number of beams increases, so it does the noise in the associated image.
- PP fail when lattice peaks are not easily detected, as it happens in the case of the appearance of sublattices in the HRTEM image. In this case, it is possible to apply some filtering to the original HRTEM image, but this may produce undesirable errors in strain determination. In these cases, GP Phase is recommended.
- PP is based in the location of peaks, and a filtering process is necessary to determine precisely their positions, while in the GP approach this filtering stage is implicit, given that a finite size window is applied in Fourier space. In both cases, researchers should be careful because local non-periodic details may be removed at this stage.

6. Conclusion

In this paper we have introduced the PP algorithm, a new real space procedure for strain mapping. While a number of algorithms working on real space have been considered, this is, to our knowledge, the first time a real space approach is useful for strain mapping around defects without user's intervention. Basically, it works on a Bragg-filtered image, locating pairs of peaks along a predefined direction and distance in the affine transformed space defined by a pair of basis vectors. This transformation greatly reduces potential errors in the determination of *partners* of a given peak. It offers the advantages of a real space approach and its behaviour is unaltered in the presence of defects as well as in the strain mapping of non-homogeneous surfaces. Nevertheless, we consider that both algorithms, GP and PP are useful for strain determination, each having different properties, advantages and pitfalls, and should be considered as complementary tools in strain mapping.

Acknowledgements

We thank M. Hÿtch for kindly providing us the basic Geometric Phase scripts. This research was supported by Spanish MEC under projects NANOSELF-II (TIC-2005-05781-C03-02) and SUSIN (MAT2004-01234), Junta de Andalucía (PAI research groups TIC-145 and TEP-0120) and network of excellence SANDiE (Contract NMP4-CT-2004-500101) of the VI European Framework Programme.

References

[1] J.M. Gibson, M.M.J. Treacy, Ultramicroscopy 14 (1984) 345.
[2] T. Walther, C.B. Boothroyd, C.J. Humphreys, Inst. Phys. Conf. Ser. 146 (1995) 11.
[3] K. Du, F. Phillipp, J. Microscopy 221 (2006) 63.
[4] M.J. Hÿtch, T. Plamann, Ultramicroscopy 87 (2001) 199.
[5] K. Tillmann, M. Lentzen, R. Rosenfeld, Ultramicroscopy 83 (2000) 111.
[6] R. Bierwolf, M. Hohenstein, F. Phillip, O. Brandt, G.E. Crook, K. Ploog, Ultramicroscopy 49 (1993) 273.
[7] P. Bayle, T. Deutsch, B. Pilles, F. Lancon, A. Marty, J. Thibault, Ultramicroscopy 56 (1994) 94.
[8] P.H. Jouneau, A. Tardot, B. Feuillet, H. Mariette, J. Cibert, J. Appl. Phys. 75 (1994) 7310.
[9] R. Kilaas, S. Paciornik, A.J. Schwartz, L.E. Tanner, J. Comput. Assist. Microscopy 6 (1994) 129.
[10] M.D. Robertson, J.M. Corbett, J.B. Webb, J. Jagger, J.E. Currie, Micron 26 (1995) 521.
[11] H. Seitz, K. Ahlborn, M. Seibt, W. Schröter, J. Microscopy 190 (1998) 184.
[12] S. Kret, C. Delamarre, J.Y. Laval, A. Dubon, Philos. Mag. Lett. 77 (1998) 249.
[13] S. Kret, P. Ruterana, A. Rosenauer, D. Gerthsen, Phys. Status Solidi (b) 227 (2001) 247.
[14] M.J. Hÿtch, E. Snoeck, R. Kilaas, Ultramicroscopy 74 (1998) 131.
[15] N. Wiener, Extrapolation, Interpolation and Smoothing of Stationary Time Series, Wiley, New York, 1949.
[16] W.H. Press, S.A. Teukolsky, W.T. Vetterling, B.P. Flannery, Numerical Recipes in C: The Art of Scientific Computing, second ed, Cambridge University Press, Cambridge, 1992.
[17] http://www.mathworks.es.
[18] http://www.uca.es/grup-invest/sic/straintool.htm.
[19] S. Kret, P. Dłużewski, J. Dłużewski, J.Y. Laval, Philos. Mag. 83 (2003) 231.
[20] A. Rosenauer, D. Gerthsen, Adv. Imag. Electron Phys. 107 (1999) 121.